



Full Length Article

Chemical ordering effect on the radiation resistance of a CoNiCrFeMn high-entropy alloy



Yangen Li^a, Jun-Ping Du^{a,b}, Peijun Yu^a, Rui Li^c, Shuhei Shinzato^a, Qing Peng^{d,*}, Shigenobu Ogata^{a,b,*}

^a Department of Mechanical Science and Bioengineering, Osaka University, Osaka 560-8531, Japan

^b Center for Elements Strategy Initiative for Structural Materials, Kyoto University, Kyoto 606-8501, Japan

^c School of Mechanical Engineering, University of Science and Technology Beijing, Beijing 100083, China

^d State Key Laboratory of Nonlinear Mechanics, Institute of Mechanics, Chinese Academy of Sciences, Beijing 100190, China

ARTICLE INFO

Keywords:

High-entropy alloy
Radiation resistance
Chemical short-range order
Defects

ABSTRACT

The chemical ordering of CoNiCrFeMn and its effect on radiation resistance is analyzed in this study via Monte Carlo (MC) annealing simulation and molecular dynamics (MD) radiation damage simulation. MC annealing at a lower temperature of 600 K forms an initial stage Cr-rich region in CoNiCrFeMn due to a strong chemical ordering-driven phase decomposition; whereas, annealing at a higher temperature of 1100 K forms a chemical short-range order (CSRO). MD radiation damage simulation shows that the Cr-rich region formed by 600 K annealing accelerates the aggregation and the evolution of defects, facilitating more dislocation loops formation. On the other hand, the CSRO structure formed by 1100 K annealing effectively delays the growth of defect number and tends to reduce the dislocation density and defect diffusion, suggesting better radiation resistance. However, the CSRO structure is destroyed by radiation, thus these advantages of CSRO will disappear in due time if CSRO cannot heal. Fortunately, since the CSRO can recover at working temperature of 1100 K, we speculate that under the working temperature of 1100 K and with a modest radiation damage rate, the advantages of CSRO can maintain for a long time. We finally discuss the condition of the CSRO preservation by proposing a CSRO radiation damage – diffusion healing competition model.

1. Introduction

High-entropy alloys (HEAs) have attracted extensive attention because of their outstanding properties such as high strength, high tensile ductility, excellent corrosion, and wear resistance [1–7]. In contrast to traditional alloys, which contain only one or two principal elements, a HEAs contains five or more principal elements; HEAs properties can also be greatly improved by adjusting the types and proportions of elements [8–12]. HEAs represent a fundamentally new alloy design concept with a broad variety of potential applications. Recently, researchers have actively explored HEAs performance in radiation damage, with several results indicating that HEAs show better radiation resistance than traditional alloys. For instance, a tungsten-based HEA was developed and showed no sign of induced dislocation loops after irradiation experiments. Furthermore, nanoindentation results of radiation-damaged materials also showed only a slight increase in hardness [13]. Using transmission electron microscopy (TEM) to

characterize dislocation loop evolution in HEAs, Lu et al. found that compositional complexity in HEAs can delay the growth of dislocation loops by reducing interstitial migration [14]. Some irradiation simulation analyses demonstrated that this sluggish diffusion effect is a key factor in HEAs' radiation resistance [15–18], while there also remained some disputes about this effect in HEAs [19,20].

Owing to its excellent radiation resistance, a promising CoNiCrFeMn HEA shows potential for application in a new generation of nuclear structure material [21,22]. However, the high-temperature working conditions above 700 K will bring another challenge for the CoNiCrFeMn as a material to be used in nuclear facilities [5,23,24]. Recently, some studies have pointed out that the chemical structure of CoNiCrFeMn, previously considered a thermally stable single-phase, seems to be chemically ordered after long-time annealing below certain temperatures [25–27]. Although the single-phase solid solution state can remain even after annealing at 1100 K or above, a Cr-rich secondary phase may form after long-time annealing at 900 K or

* Corresponding authors.

E-mail addresses: PengQing@imech.ac.cn (Q. Peng), ogata@me.es.osaka-u.ac.jp (S. Ogata).

below [25]. Therefore, additional attention should be given to the chemical ordering of CoNiCrFeMn, particularly the possible phase decomposition caused due to the high-temperature working condition experienced by materials used in nuclear facilities. Furthermore, HEAs have generally been considered to occupy a random solid solution state, but the degree of randomness of the distribution of atoms in HEAs remains to be fully determined. Some studies have reported that chemical short-range order (CSRO) structure was expected to develop after HEAs annealing at a particular temperature, with possibly significant impacts on the HEAs structural stability and mechanical properties [12,28–32]. On the one hand, both first-principles density functional theory calculation and experimental TEM observation have demonstrated that CSRO in CrCoNi has a significant relationship with stacking fault energy, so the mechanical properties of the material could be improved by tuning the degree of CSRO [33,34]. Zhao et al. also reported that defect evolution in Ni–Fe alloys may be delayed because of CSRO. In their framework, the ordered structure could influence defect migration by changing the local atomic environment, so the radiation resistance of materials could be improved by the forming of the CSRO structure [35]. On the other hand, irradiation simulation in Fe–Cr and CuNiCoFe alloys has also shown that CSRO has hardly any effect on the radiation resistance of HEAs incorporating these elements [36,37]. Thus, further study is still needed regarding CSRO formation in HEAs and the influence of CSRO on mechanical properties, especially radiation resistance.

To systematically investigate the chemical ordering effect on the radiation resistance of CoNiCrFeMn at high working temperature, Monte Carlo (MC)–Molecular Dynamics (MD) hybrid annealing simulations at various temperatures followed by MD irradiation simulations were performed to the annealed samples. The MD simulation is a well-established approach for investigating irradiation, such as radiation damage and cascades phenomena [38]. As an efficient and reliable approach, materials simulation plays an important role in the exploration of material properties [39]. Here, we confirmed that the formation of initial stage Cr-rich regions after annealing at 600 K reduced the radiation resistance of CoNiCrFeMn. The CSRO structure after annealing at 1100 K enhanced radiation resistance, but the enhancement did not persist long because of CSRO destruction under irradiation. Our investigation suggests that the chemical structures of HEAs including CSRO and its formation temperature should be carefully evaluated, especially when it is used as a radiation resistance material at various working temperatures, because if the CSRO formation temperature can be adjusted to the working temperature, radiation damage rate can be set as a modest value, and accelerate the CSRO formation rate by controlling, for example, HEA chemical compositions, then further radiation resistance may be achieved.

2. Method and models

A 2-NN modified embedded atom method potential was chosen to describe the interatomic interactions of all the atoms in the CoNiCrFeMn [40]. The short-range repulsion parameters were adjusted according to the findings of Hyeon-Seok et al., ensuring sufficient short-range repulsion for irradiation simulations and with little effect on physical properties [22]. This potential has been successfully applied to previous irradiation simulations and has predicted the mechanical properties in nonequilibrium HEAs [16,22]. In order to compare with their results, the same irradiation simulation method was used without considering electronic stopping, which proved to have little effect in complex materials (e.g. MEA/HEA) [41]. We also verified the formation of other intermetallic phases by using this potential, details could be found in the Supplementary Information Fig. S1. OVITO was used to analyze and visualize the simulation results [42]. The Wigner–Seitz method was used to count the number of defect atoms [43]. The dislocation extraction algorithm method was used to identify the dislocation loops [44].

The hybrid MC–MD simulations were conducted to obtain the model with different initial CSRO state after annealing at various temperatures.

There were 10 MC steps for each MD step, for a total of 5 million MC steps, with an average of 20 swaps per atom. Warren–Cowley parameter α_n^{ij} was used to evaluate the degree of CSRO for all the element pairs after annealing at the different temperature [45].

$$\alpha_n^{ij} = 1 - \frac{P_n^{ij}}{C_j}, \quad (1)$$

where i and j refer to the elements, and n refers to the n th nearest neighbor. P describes the probability of occurrence of each element as a surrounding atom, and C is the systemwide mean concentration of the corresponding element. CSRO parameters have expected values of 0 when all atoms are completely randomly distributed. In this study, temperatures of 600 K and 1100 K were chosen as annealing temperature, and MC–MD hybrid annealing simulation for each temperature was conducted. Fig. 1 shows local atomic structures of CoNiCrFeMn, after annealing at (a) 600 K, (b) 1100 K, and (c) a random element distribution. All models have fcc structure with an average lattice constant of 3.57 Å, and total number of atoms is 256,000 in a cubic shaped simulation box with a length of 14.28 nm on each side and periodic boundary condition in each side. Each atomic element has the same number of atoms. CSRO parameters for each element pair in the model with three different initial CSRO states were determined and are shown in Fig. 1 (d). The CSRO parameters of CoNiCrFeMn differed with annealing temperatures. At 600 K, Co–Cr and Cr–Fe atom pairs were strongly mutually repulsed and showed segregation (i.e., positive parameters). By contrast, Co–Fe, Ni–Mn, and Cr–Mn atom pairs exhibited mutual attraction and showed a tendency to cluster (i.e., negative parameters). The chemical ordering of different element pairs in CoNiCrFeMn was consistent with previous simulation results by Guo et al. [46]. During the annealing process, no crystal structure phase transition occurred (for instance, fcc to bcc or hcp). We found the formation of Cr-rich regions in CoNiCrFeMn, which is consistent with the results from previous work by Otto et al. [25]. When CoNiCrFeMn annealed at 600 K, a Cr-rich region formed because of the phase decomposition. It should be noted that in the experiments by Otto et al., because of the long-time annealing, Cr tends to form a bcc-phase at grain boundaries or intragranular inclusions. However, due to simulation limitations, we only consider short-time annealing in the perfect matrix structure, and this Cr-rich region is still in the initial stage, with no phase transition. Others have also been interested in the effect of this initial Cr-rich region on the properties of CoNiCrFeMn [48]. A higher annealing temperature of 1100 K weakened the separation of Co–Cr and Cr–Fe, as well as the clustering tendencies of Co–Fe, Ni–Mn, and Cr–Mn. At a higher temperature, the Cr–Cr parameter decreased in value, and the Cr-rich region disappeared. After annealing at a high temperature of 1100 K, all the CSRO parameters were much lower in value than after annealing at 600 K. However, significant CSRO structure, rather than phase separation was still evident after annealing at a high temperature of 1100 K. The CSRO parameter values of the model with random CSRO state were all found to be close to 0, demonstrating that all elements were randomly distributed.

Atomic structure of the models was relaxed at 700 K for 100 ps using NVT ensemble MD simulation before starting the irradiation simulations. All of the atomic simulations in this study were performed by using large-scale atomic/molecular massively parallel simulator (LAMMPS) code [47]. The primary knock-on atoms (PKA) were randomly chosen with the energy of 5000 eV in the model, and the random direction of the motions of all PKA were implemented to achieve a homogeneous irradiation effect. The irradiation process was conducted by imbuing each PKA atom with a randomly directed velocity corresponding to this energy. An adaptive time step was used to ensure that any atom will not move more than 0.002 nm in each simulation step. Three runs with different random seeds for each condition were performed and averaged. Microcanonical ensemble was applied during the irradiation simulations, and Berendsen thermostat [48] with 700 K

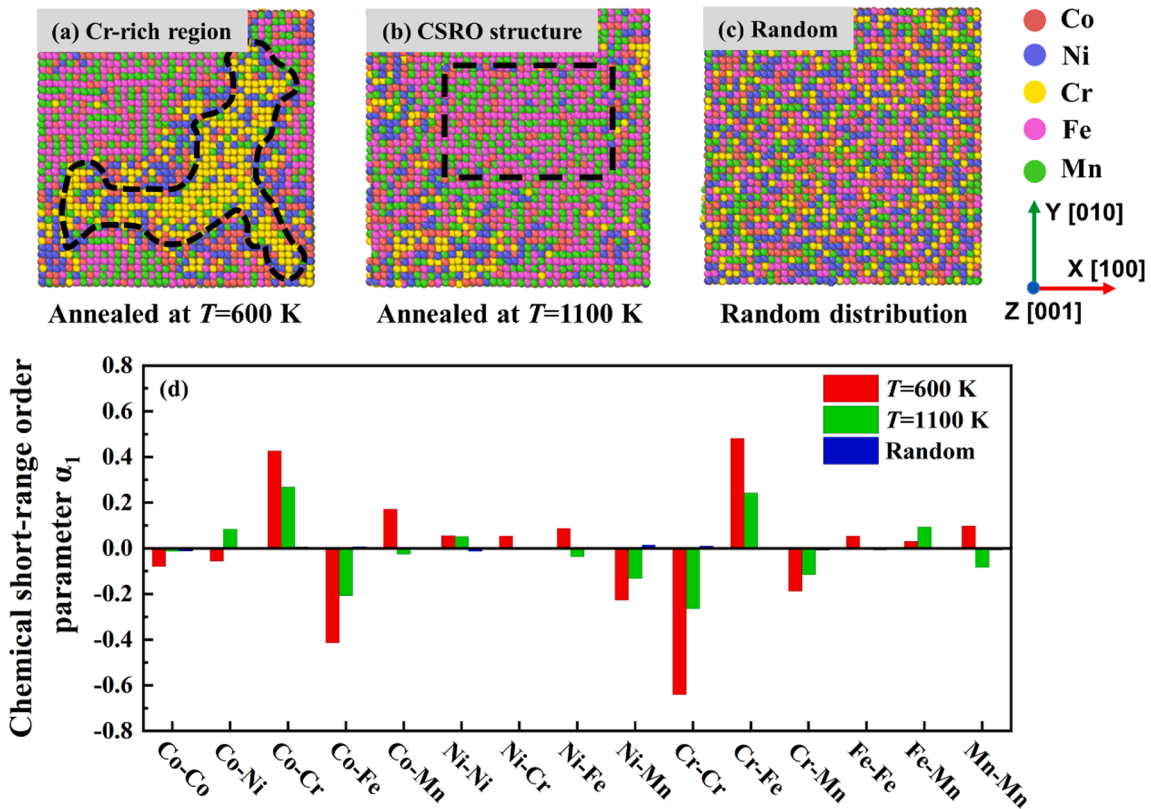


Fig. 1. (a)–(c) Local structural characteristics in CoNiCrFeMn after annealing at a temperature of (a) 600 K and (b) 1100 K and (c) in the random states, respectively. (d) Chemical short-range order parameters of various element pairs.

was applied only with 1-nm-thick layer regions on all sides to mimic the severe high temperature working conditions. It is worth noting that many irradiation experiments and simulations were also performed at around 700 K [15,22]. Each irradiation bombardment lasted for 50 ps to ensure the model could cool down to the ambient temperature. Considering the available computational resources and time, the irradiation process contained 500 times of bombardments. According to the NRT displacement model, the final damage level can reach a dose of 0.1 dpa. This dose of radiation damage level also has been well used to study the radiation resistance of materials before [49,50].

3. Results

3.1. Irradiation simulation

Five hundred consecutive irradiation bombardments were conducted in the model with three different initial CSRO states. Fig. 2 shows the structural damage and dislocation loops formation after 100, 300, and 500 irradiation bombardments, and the corresponding damage levels were 0.02, 0.06, and 0.1 dpa, respectively. A threshold displacement energy of 40 eV was used here, which is consistent with previous similar simulations and experiments [18,51]. No phase transition occurred during the irradiation process, and several defects gathered into clusters. Because of irradiation bombardment and defect cluster evolution, dislocations were found in the model with different initial CSRO states. Most of the dislocations occurred in the form of complex dislocation loops, mainly represented by interstitial-type dislocation segments with the Burgers vectors of $b = 1/6 \langle 112 \rangle$. We only found few vacancy-type dislocation loops with the Burgers vectors of $b = 1/6 \langle 110 \rangle$, some of which will transform into stacking fault tetrahedral dislocations or voids during the irradiation simulation. Therefore, HEAs can inhibit the formation of void defects and enhance radiation resistance [15].

To further evaluate the performance of HEA with different initial

CSRO states during irradiation bombardment simulation, we statistically analyzed the defect concentration, interstitial cluster size distribution, dislocation density, and average dislocation loops length. Results for each initial CSRO state were obtained from the average of three simulations with different random seeds.

Fig. 3 (a) shows the defect concentration computed by Wigner-Seitz method as a function of the number of bombardments. The model with different initial CSRO states showed a similar initial tendency toward a rapid increase of defect concentration. Because of the dynamic balance between the generation of new defects and the annihilation of interstitials and vacancies, defect concentration then saturated and fluctuated around a stable value, this trend could also be found in other HEA/MEA radiation results [18,49]. Compared with other initial CSRO states, the model after annealing at 1100 K showed a relatively lower defect concentration and maintained a slow increase in defect concentration during the simulation. Only after approximately 400 irradiation bombardments the defect concentration gradually reached the level similar to that reached by the model with other initial CSRO states.

Fig. 3 (b) shows the size distribution of interstitial defects clusters after 500 irradiation bombardments. The first-nearest-neighbor distance (2.5 Å) was used as the cluster identification criterion, and all interstitial atoms within this distance were considered to belong to the same defect cluster. The error bars represent the upper and lower deviation of three irradiation simulation results. In each initial CSRO state of the model, most of the interstitial defects (40 % or more) existed in the form of the medium-size cluster (between 11 and 30 defects per cluster). Notably, super-large-size clusters (larger than 100 defects per cluster) occurred more (approximately 15 % of all defects) in the model after annealing at 600 K than in the others; this finding indicates a faster evolution of defect clusters in that initial CSRO state.

Fig. 3 (c) shows the dislocation loops density for each different initial CSRO state in the model; fluctuating growth was maintained during all irradiation bombardments. However, higher dislocation loops density

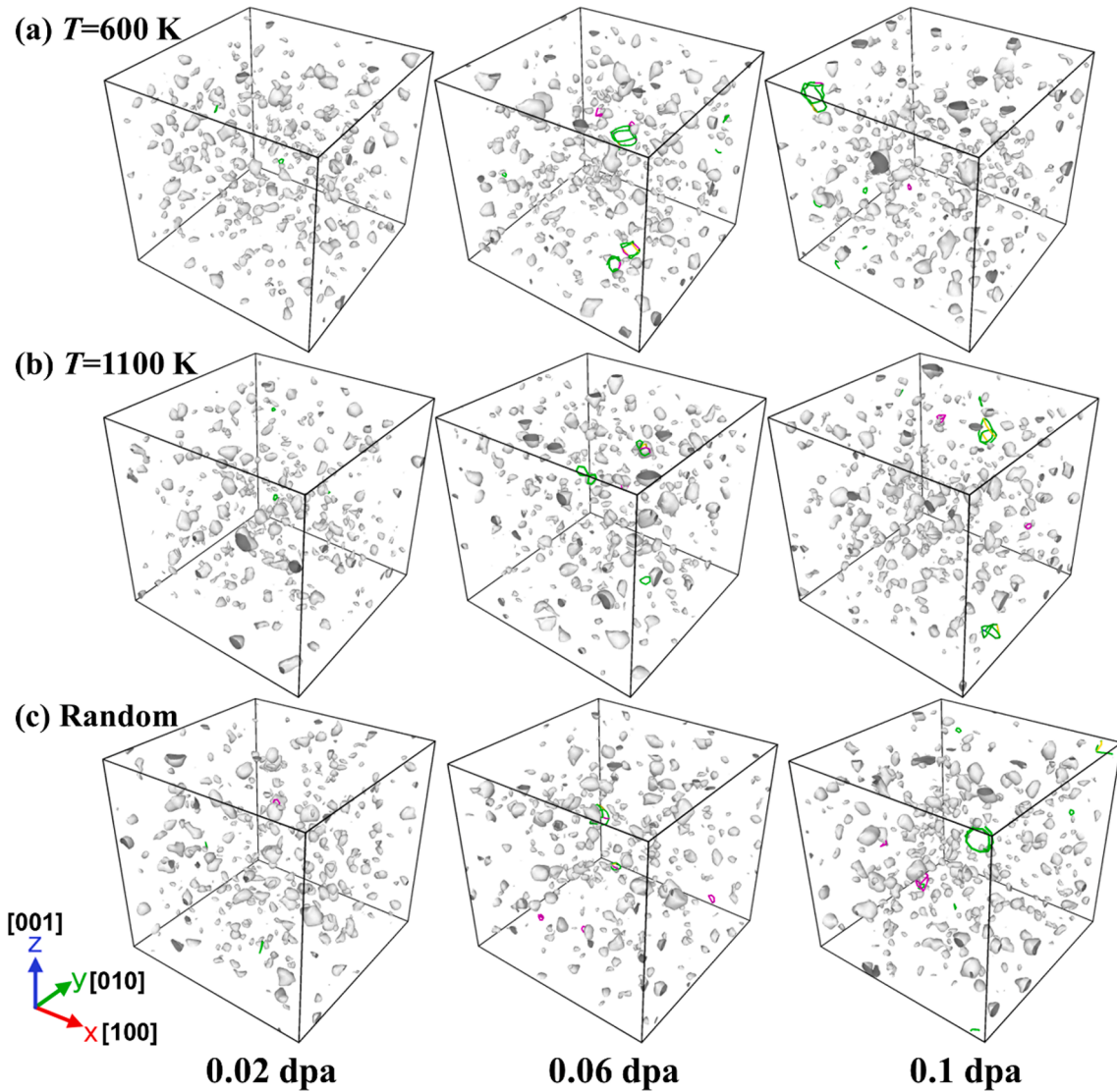


Fig. 2. (a)–(c) Structural damage and dislocation loops in CoNiCrFeMn after annealing at a temperature of (a) 600 K and (b) 1100 K and (c) in the random states, respectively. Green, pink, and yellow lines denote Shockley 1/6 <112>, Stair-rod 1/6 <110>, and Hirth 1/3 <100> dislocation loop segments, respectively. (For interpretation of the references to colour in this figure legend, the reader is referred to the web version of this article.)

mostly occurred in the model after annealing at 600 K, since more of the total interstitial defects were gathered in super-larger-size clusters. Compared with others, the model after annealing at 1100 K showed a substantially delayed increase in dislocation density.

Fig. 3 (d) shows the average dislocation loops length during irradiation bombardment. The average dislocation loops lengths of the model with three initial CSRO states ranged from 10 Å to 17 Å. Although dislocation evolution sometimes increased the average dislocation loops length over time, average dislocation loops length decreased rapidly with the decomposition of dislocation because of the instability of large-size dislocation loops in HEAs. As found in our previous study, this HEA feature differed starkly from those of traditional metals. For example, in pure Ni, large-size dislocation loops are generated and exist stably in the form of Frank 1/3 <111> dislocation loops [16].

The above findings demonstrated that the annealing temperature of CoNiCrFeMn, acting via the CSRO level, influenced defects and dislocation loops performance during irradiation. The model after annealing at 600 K showed faster evolution of defect clusters, resulting in higher dislocation loops density. The model after annealing at 1100 K showed delays in defect growth and dislocation loops formation during irradiation bombardment, amounting to improved radiation resistance. The

effect of annealing temperature on CoNiCrFeMn properties deserves additional attention.

3.2. Defect evolution

Defect evolution simulations were conducted to determine the reason for elevated dislocation loops density in the CoNiCrFeMn model after annealing at 600 K. As shown in Fig. 4, 1% Frenkel pairs were randomly added into a small-size model of 32,000 atoms. The total simulation time was 10 ns, and the same simulation was done in the model with a random CSRO state for comparison. At first, all defects were randomly distributed in the form of small-size clusters of point defects. During defect evolution simulations, some interstitials gathered into larger clusters, whereas some disappeared via the combination with vacancies. The results after 5 ns of evolution show that complex dislocation loops formed quickly in the model after annealing at 600 K. However, all defects still existed as clusters in the model with random CSRO state, and no dislocation loops could be found. Finally, dislocation loops were stable in the model after annealing at 600 K, whereas defects in the model with random CSRO state occurred in the form of larger-size clusters. The whole process of defect evolution in the model after

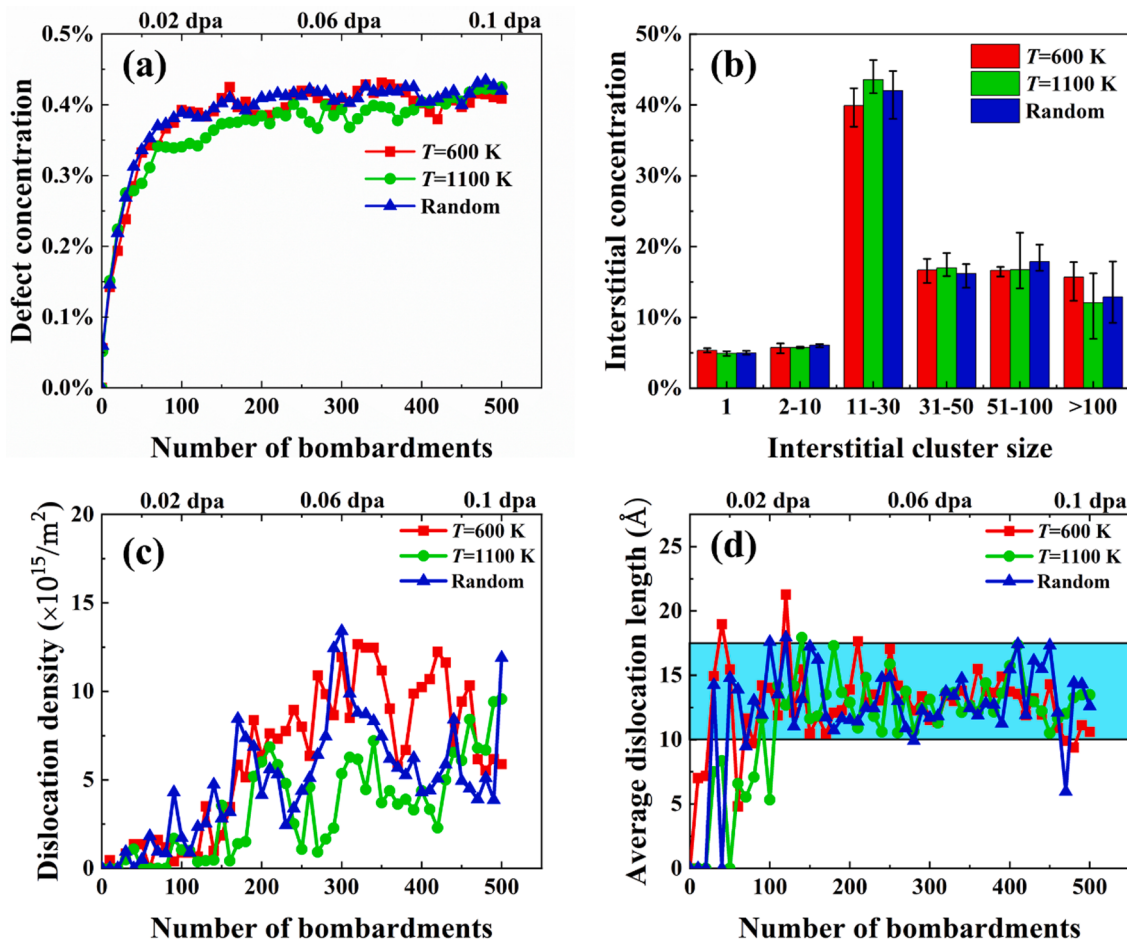


Fig. 3. (a) Defect concentration during the bombardment; (b) interstitial concentration distribution of cluster size, (c) dislocation loops density, and (d) average dislocation loops length.

annealing at 600 K can be found in Supplementary Movies 1. We note that the dislocation loops formation region was in the Cr-rich region, this finding implies that dislocations are easier to form in the Cr-rich region. To confirm this, we compared prismatic dislocation loop energy in Cr-rich with that in Cr-less regions (Supplementary Information Fig. S2) and found the former has lower energy. The aggregation of interstitials and defect clusters evolution made it easier for dislocation loops to form here. The Cr-rich region associated with annealing at 600 K seems to have accelerated dislocation loops growth, diminishing the radiation resistance of CoNiCrFeMn.

3.3. Thermodynamics behavior after irradiation

The thermodynamic behavior of these defect structures following irradiation bombardments is also interesting. As a result, hybrid MD–MC annealing simulations on nonequilibrium systems were repeated to investigate the further evolution of defects. The potential energy change during annealing simulations was depicted in Fig. 5 (a). This potential energy gradually decreased and eventually reached the equilibrium state in the model with Cr-rich ($T = 600$ K) and CSRO ($T = 1100$ K). Before and after annealing simulation, the potential energy per atom in the model with Cr-rich (CSRO) was -3.962 (-3.959) eV/atom and -3.973 (-3.972) eV/atom, respectively. Fig. 5 (b), (c), (d), and (e) show the distribution of defects before (nonequilibrium stage) and after annealing (equilibrium stage). Fig. 5 (f) depicts a change in the defect composition of elements. The Cr and the Mn atoms of defects in the equilibrium state structure increased by annealing. In particular, we investigated the composition of the largest-size defect cluster in the

model with Cr-rich and CSRO. The total proportion of Cr and Mn atoms in the largest-size defect cluster in the model with Cr-rich and CSRO, as shown in Fig. 5 (g), reached approximately 50 % and 60 %, respectively. It was discovered that Cr and Mn are the fastest diffusing atoms in CoNiCrFeMn, preferring to aggregate on the defect position [17]. This is because Cr and Mn atoms nucleate and form new phases at the grain boundary and defect more quickly [25].

4. Discussion

The formation of dislocation loops during irradiation simulations was mainly related to the aggregation of interstitials and the evolution of clusters. To study the influence of annealing temperature on radiation resistance in CoNiCrFeMn, interstitial defect diffusivity must be calculated. The mean square displacement $\langle r^2(t) \rangle$ of a single interstitial defect was calculated, allowing the diffusivity D of the interstitial to be estimated by [52]:

$$D = \frac{\langle r^2(t) \rangle}{2nt}, \quad (2)$$

where n ($n = 3$) is the dimensional diffusion of an interstitial defect and t is time. Fig. 6 (a) showed the diffusivity of an interstitial defect in CoNiCrFeMn after annealing at 600 K, 1100 K, and in the random state. The error bars represent the upper and lower deviation of interstitial diffusivity at different initial positions. The diffusivity of an interstitial defect in CoNiCrFeMn after annealing at 600 K and 1100 K varied significantly (from 2.74×10^{-3} Å²/ns to 1.22×10^{-6} Å²/ns and from 6.05×10^{-4} Å²/ns to 2.83×10^{-7} Å²/ns, respectively.) and was strongly

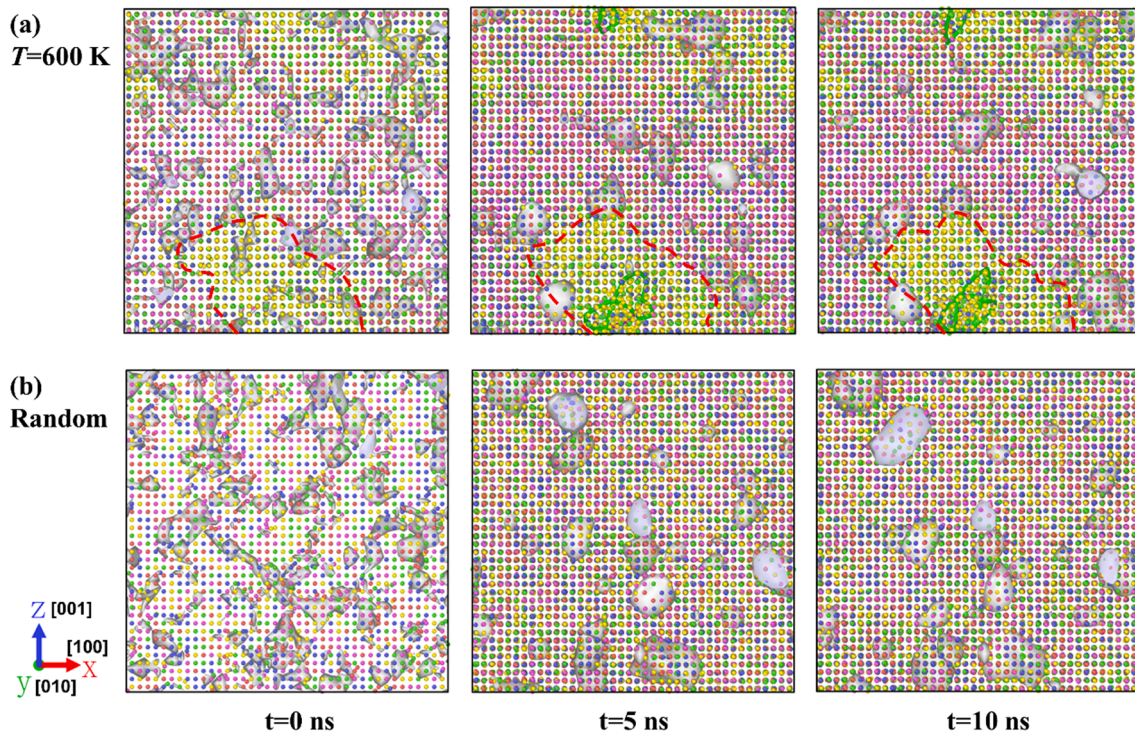


Fig. 4. Evolution of 1 % Frenkel pairs in CoNiCrFeMn throughout 10 ns. (a) Model after annealing at 600 K and (b) random states. The colors of line segments denote different types of dislocation loops as described earlier. The red dashed lines added as a guide for the eye and marked the Cr-rich region. (For interpretation of the references to colour in this figure legend, the reader is referred to the web version of this article.)

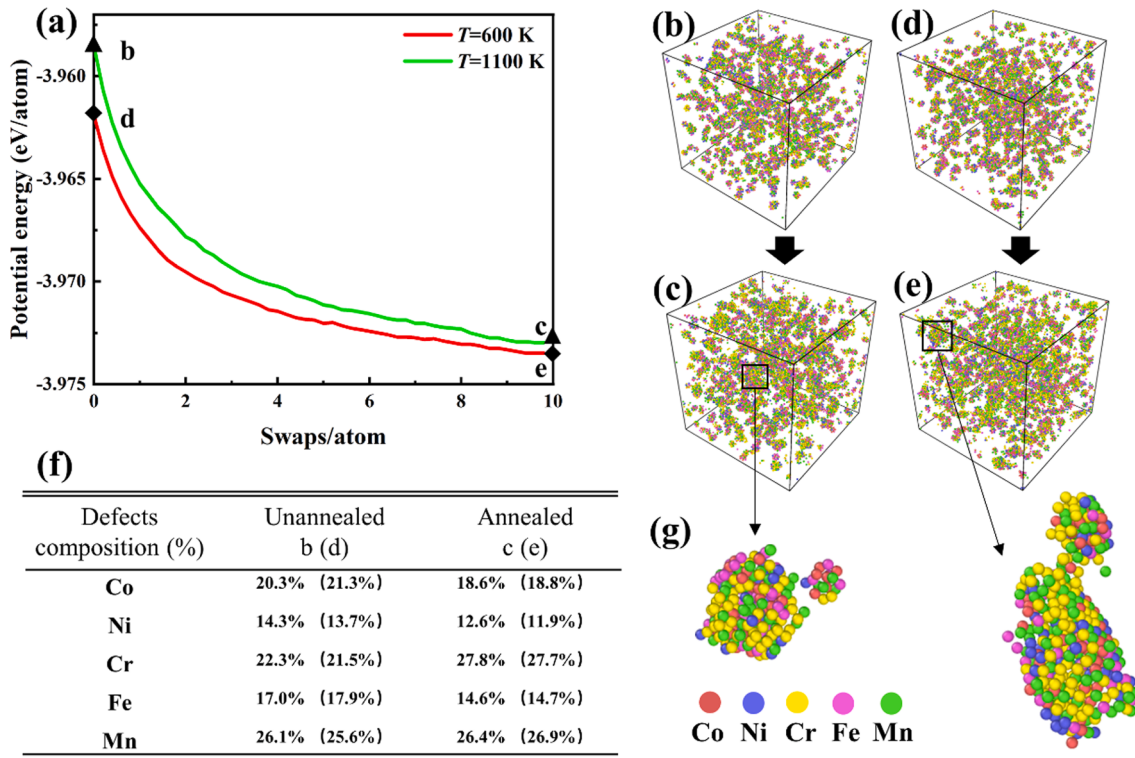


Fig. 5. (a) Potential energy change during MD–MC annealing; (b)–(e) defect distribution in the model before and after annealing; (f) defect composition of elements before and after annealing; (g) largest cluster in the model after annealing.

influenced by the local environment. However, because of the more homogeneous atomic environment, the interstitial diffusivity in the model with random state was relatively stable. Furthermore, we

discovered that the diffusivity of an interstitial was higher in the model after annealing at 600 K but lower in the model after annealing at 1100 K. This is because the formation of Cr-rich changes the diffusion method

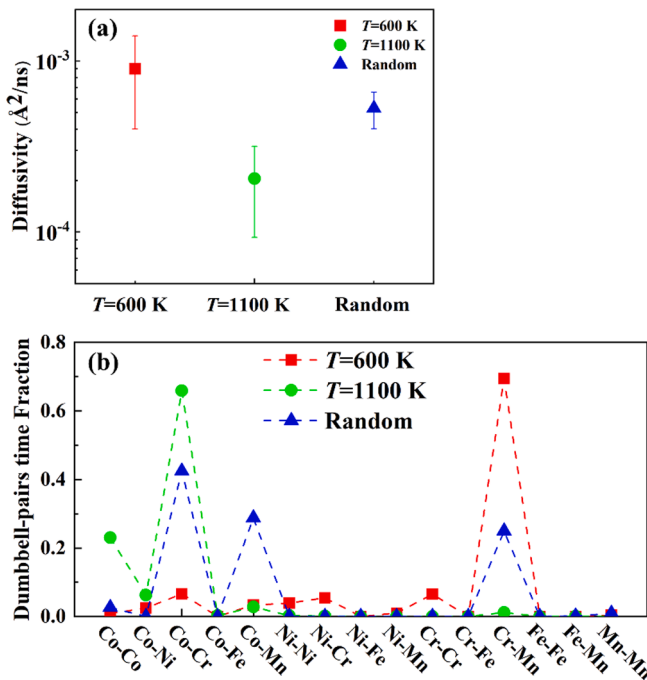


Fig. 6. (a) Interstitial defect diffusivity and, (b) time fraction of different interstitial dumbbell pairs during diffusion in the model with three different initial CSRO states.

of the interstitial, as discussed below, and CSRO structure delays defect diffusion, which is consistent with the findings from related studies by Zhao et al. [35]: The preferential diffusion effect of CSRO structure may influence interstitial diffusion, resulting in considerable delays in defect evolution. We also tracked the time fraction spent by different interstitial dumbbell pairs in CoNiCrFeMn during diffusion because the interstitial forms different dumbbell pairs during diffusion. The Wigner–Seitz method was used to identify the location of the interstitial defect during the diffusion process, and the perfect structure lattice site served as the reference configuration [45]. When interstitial and lattice atoms occupied the same lattice site, they were referred to as an interstitial dumbbell, and the statistical results are shown in Fig. 6. (b). It is interesting to note that in the model with random state, interstitial diffusion was primarily via the Co–Cr, Co–Mn, and Cr–Mn dumbbell pairs motions. However, in the model with CSRO, the Co–Cr dumbbell pair dominated the interstitial motion, and in the model with Cr-rich, the Cr–Mn dumbbell pair dominated. It is shown that interstitial diffusion is highly dependent on their local chemical environment, which changes the dumbbell proportion.

We further studied the interstitial diffusion in the model with Cr-rich. In some runs, the interstitial defect showed rapid diffusion with high diffusivity, but in other runs, the defect was almost stagnant. Indeed, three different interstitial diffusion scenarios occurred in the runs of the model after annealing at 600 K. First, when the interstitial was located near the Cr-rich region boundary, the interstitial was absorbed by the phase boundary and resisted further movement. Second, when the interstitial was away from the Cr-rich region boundary, the interstitial showed the same diffusivity as in other HEA. Finally, when the interstitial was in the Cr-rich region, it is expected to form more Cr–X interstitial dumbbell pairs during diffusion. Fig. 6 (b) showed the time fraction spent by different interstitial dumbbell pairs during diffusion, it is obvious that more Cr–Mn dumbbell pairs formed in the model with Cr-rich. This is because of the smaller formation energy of [001] Cr–Mn dumbbell in CoNiCrFeMn [53]. In addition, we calculated the migration barrier of Cr–Mn interstitial dumbbell with different Cr concentrations by DFT with nudged elastic band method [54,55], where higher Cr concentration led to lower interstitial dumbbell migration barrier (the

details of DFT calculation and results are provided in the Supplementary Information Fig. S3). The same phenomenon has also been found in Ni–Fe alloys before; Osetsky et al. found that with the increase of Fe concentration, interstitial diffusivity gradually increases because the Ni–Ni interstitial dumbbell transforms into Fe–Fe dumbbell [56]. Therefore, the rapid diffusion phenomenon of interstitial in the model with Cr-rich could be explained by the dumbbell type transition. Hence, the formation of the Cr-rich region in CoNiCrFeMn after annealing at 600 K imbued the local environment of the interstitial defect with a considerable influence on diffusivity. The additional details of the interstitial diffusion in the model annealed at 600 K can be found in Supplementary Movies 2–4.

Overall, the Cr-rich region in CoNiCrFeMn whose formation had been induced by annealing at 600 K causing changes in elemental distributions. These changes caused more Cr–X interstitial dumbbells to form in the Cr-rich region and led to the fast migration of interstitials, resulting in less reliable radiation resistance performance. Additionally, the CSRO structure formed in CoNiCrFeMn after annealing at 1100 K appeared to reduce interstitial defect diffusivity and delay defect evolution. This effect of CSRO on interstitial diffusion is expected to be reflected in the radiation resistance performance of CoNiCrFeMn. For these reasons, significant attention should be paid to the effect of annealing temperatures on the element segregation of CoNiCrFeMn, especially the effect of Cr-rich region on the properties of CoNiCrFeMn after annealing.

As aforementioned, the radiation resistance of CoNiCrFeMn after annealing at 600 K was worse because of the faster evolution of defect clusters in the Cr-rich region and consequently higher dislocation loops density. The mechanism of the effect of the Cr-rich region on defect evolution thus demands further study. Diffusion simulations of two interstitial defects throughout 10 ns with distinct initial defect positions were performed on a small-size model of 4000 atoms to observe the effect of the Cr-rich region on defect evolution. As shown in Fig. 7, the interstitial in the top part of the model, where all kinds of atoms were nearly randomly distributed, showed slow diffusive and resisted long-distance migration. However, the interstitial in the bottom part of the model, where the Cr-rich region formed, showed rapid diffusion. After approximately 5.5 ns, the two interstitials met at the phase boundary, where they merged and entered the Cr-rich region. The details of interstitial diffusion can be found in Supplementary Movie 5. The lattice constants of the top and bottom parts of the model were calculated to be 3.60 and 3.65 Å, respectively. The lattice misfit degree between the two parts was calculated as 1.38 % according to:

$$\delta = \frac{2(a_2 - a_1)}{a_1 + a_2}, \quad (3)$$

where a_1 and a_2 are the lattice constants of the two phases. This minute lattice misfit indicates that the two phases can form a coherent interface capable of stable persistence. However, the large lattice constant of the Cr-rich region also affected defect diffusion, and the internal stress caused by the lattice misfit may have provided part of the driving force for defect diffusion, facilitating the gathering of defects in the Cr-rich region. These results demonstrate the unique defect aggregation mechanism in CoNiCrFeMn after annealing at 600 K, namely, the occurrence of a Cr-rich region and the consequent lattice misfit that provide part of the driving force for the defect diffusion. The gathered interstitial defects then entered the Cr-rich region and merged with other defects. This unique interstitial aggregation mechanism indicates that the formation of the Cr-rich region accelerated defect aggregation and growth, resulting in higher dislocation density during the irradiation simulation.

Additionally, the difference in local interstitial formation energy may contribute to the difference in interstitial aggregation mechanisms. For the fcc lattice, interstitials remain at the octahedral vacancy sites and then form an interstitial dumbbell with a lattice atom in the [100] direction. Fig. 8 (a) shows such an interstitial dumbbell and the

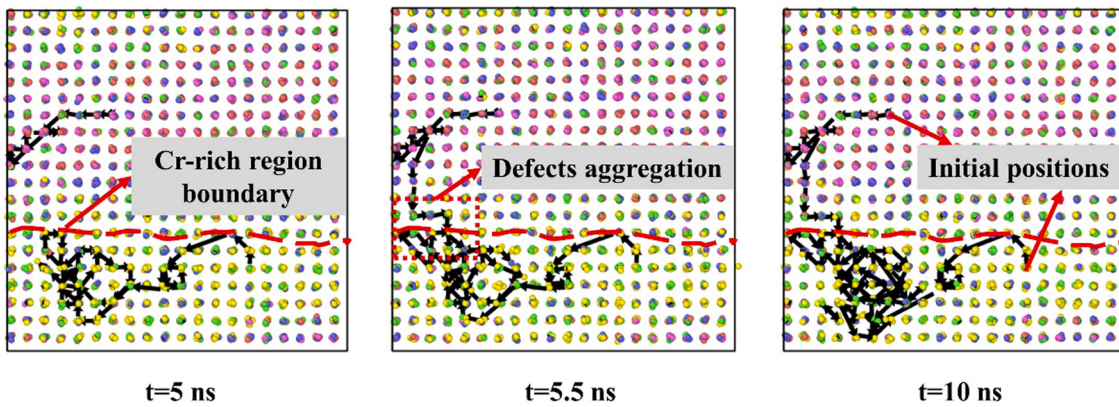


Fig. 7. Diffusion simulation of two interstitial defects with distinct initial positions in CoNiCrFeMn after annealing at 600 K. Black lines denote the diffusion trajectories of interstitials; red dashed lines denote the Cr-rich region boundary. (For interpretation of the references to colour in this figure legend, the reader is referred to the web version of this article.)

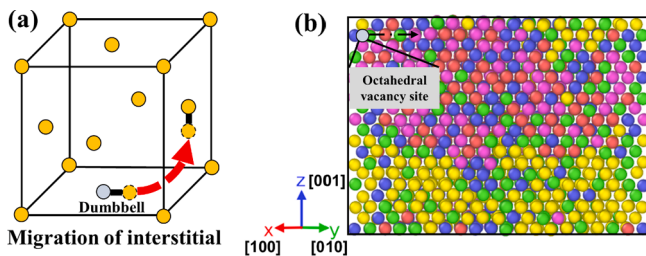


Fig. 8. (a) Interstitial [100] dumbbell and migration mechanism in fcc lattice. (b) (110) CoNiCrFeMn plane after annealing at 600 K.

migration mechanism of the interstitial. The interstitial migrates along with the dumbbell in the [100] direction to a new octahedral vacancy site and then forms another interstitial dumbbell to complete the interstitial migration. Therefore, the migration direction of the interstitial depends on the formation energies of interstitial dumbbells. As shown in Fig. 8 (b), to determine the interstitial formation energy for various sites, the (110) plane was selected for the calculate of the local interstitial formation energy. For each octahedral vacancy site, we inserted an interstitial atom and then calculated the corresponding energy after the interstitial forms a dumbbell pair with surrounding lattice atoms. Finally, we can obtain the interstitial formation energy in the (100) plane. The interstitial formation energy was calculated according to:

$$E_I^f = E_I - E_{\text{perfect}} - \mu, \quad (4)$$

where the E_I is the total energy of the structure containing the interstitial, E_{perfect} is the energy of a perfect lattice, and μ is the chemical potential of the corresponding element in CoNiCrFeMn. The details of defect formation energy calculation can be found elsewhere [53].

To illustrate the difference in local interstitial formation energy, we plotted contour maps of interstitial formation energy across different octahedral vacancy sites in the (100) plane. Fig. 9 (a)–(e) shows the interstitial formation energy results for each element of CoNiCrFeMn. To quantify the Cr-rich region boundary, the Cr element chemical concentration in a region (within a sphere with a radius of 6 Å) around each atom was calculated. In this case, Cr element chemical concentration C_{Cr} greater than 0.3 is identified as a Cr-rich region, less than 0.2 is identified as atoms random distribution region, and the boundary is between those two values. This approach was also used in our previous study [57]. The interstitial dumbbells formation energy for each element of CoNiCrFeMn differed across octahedral vacancy sites because of elemental distribution change after annealing at 600 K. Fig. 9 (f) shows the average interstitial formation energy in the [001] direction of the

(110) plane; the Cr-rich region showed significantly lower dumbbells formation energy for all five elements of CoNiCrFeMn. These results could also explain the easier formation of dislocations in the Cr-rich region since defects tended to gather in this region.

It has also been reported that CSRO structure imbues good radiation resistance by slowing the diffusivity of defects, thus delaying the defect evolution and suppressing defect growth [30,35]. In our model, annealed at 1100 K produced a CSRO structure, and the aggregation of interstitial clusters was the main cause of dislocation formation during irradiation bombardment. Therefore, defects cluster in CoNiCrFeMn annealed at 1100 K were expected to be smaller than in the other states, and dislocation loops were also expected to be fewer. In our irradiation simulations, the model exhibiting CSRO did show slower average interstitial defect diffusivity and lower defect concentration. The defect cluster size statistic also showed that CSRO could suppress the total number of defects accruing to super-large-size clusters so that more defects instead occurred in middle-size clusters. However, the lower defect concentration in model runs exhibiting CSRO state was only temporary; after approximately 300–400 bombardments, the defect concentration reached that of the model with random state. This may be because of the damage of CSRO structure during radiation.

Fig. 10 (a)–(c) shows the changes in CSRO parameters for key element pairs in irradiation bombardment simulation with three different initial states of CSRO. Here, it is worth noting that the irradiation bombardment is a fast process. All the atoms in the radiation region are immediately melted and rearranged within 10 ps after each bombardment. The thermal activation time of CSRO is several orders of magnitude longer than that destroyed by the radiation bombardments. Hence, there is almost no nonlinear interaction between these phenomena, and we can think that the changes of CSRO in Fig. 10 are dominated by bombardment during irradiation simulation (details could be found in Supplementary Information). It is interesting to find that the CSRO parameters for each element pair tended to be stable. As for the model with random state, CSRO parameters showed some changes, but they remained low in magnitude when compared with the corresponding parameter values of model in other initial states. We would predict that with additional irradiation bombardments and if without healing mechanism of CSRO, the three different initial states of CSRO parameter values would eventually converge, since irradiation bombardment progressively destroys the CSRO structure. Hence, although the model runs exhibiting CSRO showed low defect concentrations during initial stage, irradiation bombardment would continue to destroy CSRO structure. Defects would be expected to continue increasing in number, finally reaching the same profusion as in the model with initial random state. For this reason, the enhanced radiation resistance effect of CSRO does not last for long.

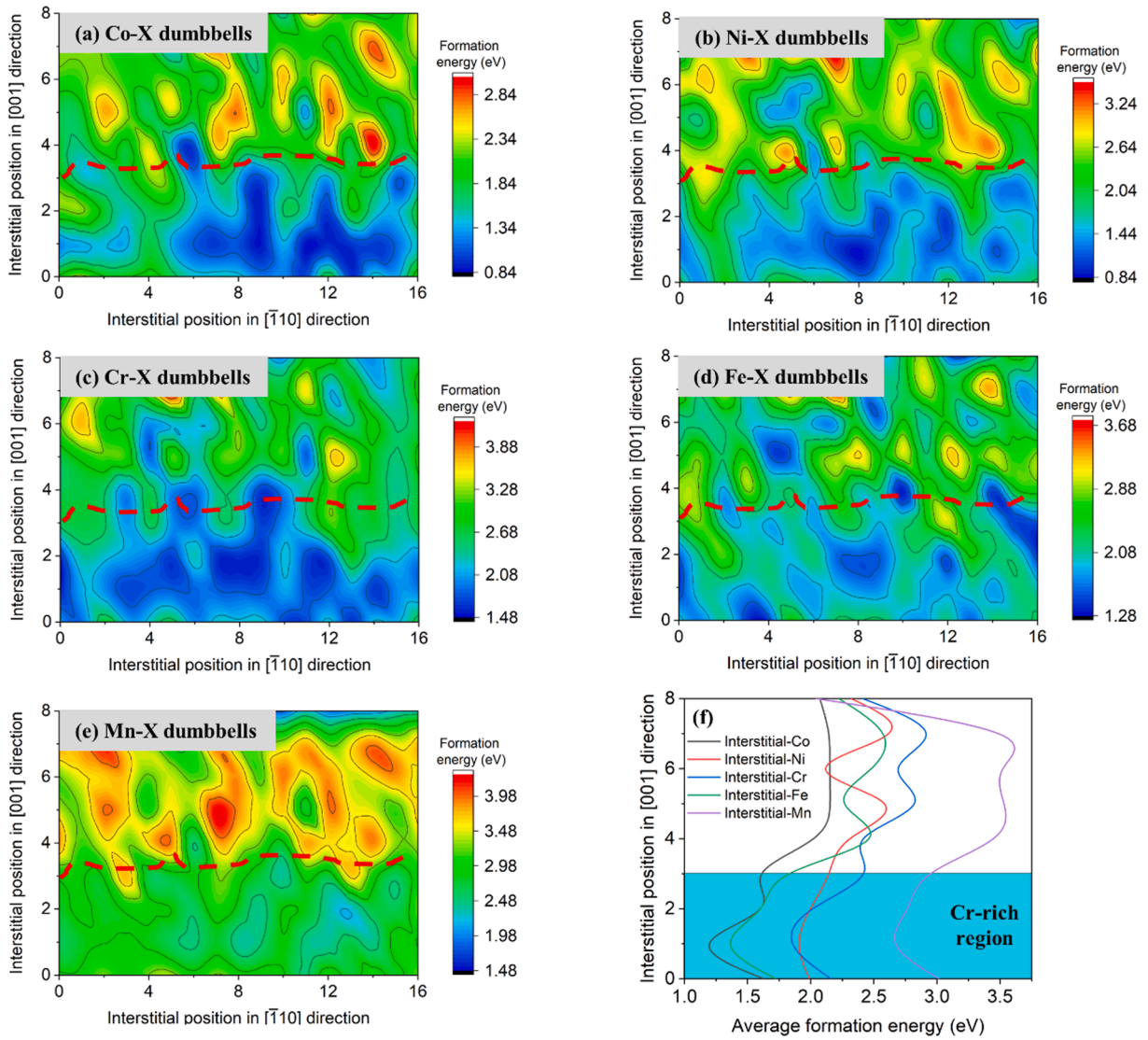


Fig. 9. (a)–(e) Formation energy of interstitial dumbbell pairs of (a) Co–X, (b) Ni–X, (c) Cr–X, (d) Fe–X, and (e) Mn–X in the (110) plane; red dashed lines denote the region boundary. (f) Average formation energy change of interstitial in [001] direction of each element. (For interpretation of the references to colour in this figure legend, the reader is referred to the web version of this article.)

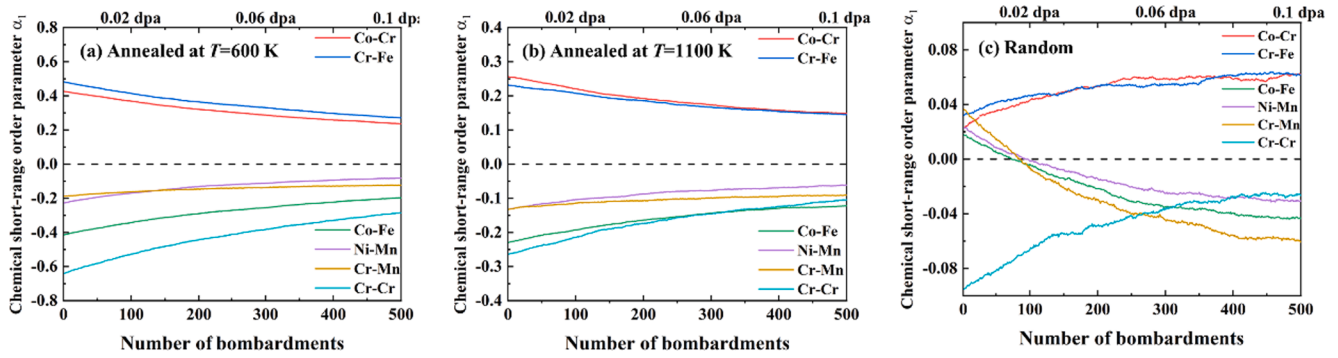


Fig. 10. Changes in chemical short-range order parameter values for CoNiCrFeMn during irradiation bombardment for (a) annealing at 600 K, (b) annealing at 1100 K, and (c) a random state.

However, we can obtain the CSRO healing mechanism if the working temperature is elevated to 1100 K. The CSRO structure formed by annealing at 1100 K must be thermodynamically stable at 1100 K. Therefore, we still have a chance to preserve the advantages of the

radiation resistance of CSRO for a long time by controlling the working temperature and radiation bombardment. To show the possibility of CSRO preservation, the competition between radiation damage rate and CSRO healing (re-formation) rate at the working temperature should be

discussed. Since the CSRO healing proceeds by thermally activated atomic diffusion through vacancy and interstitial jumps, the time scale of CSRO healing is provided by the frequency of the vacancy and interstitial jumps [57]. For simplicity, we only consider the interstitial jump as the CSRO healing mechanism in the following discussion because the interstitial diffusion is much faster than the vacancy diffusion. The CSRO parameter α_1 is representatively used to describe CSRO state.

We propose a CSRO radiation damage – diffusion healing competition model as schematically shown in Fig. 11 (a). The dash lines of $\alpha_1^E(T^W)$ and α_1^D shows the CSRO parameter α_1 at an equilibrium CSRO state after long-time annealing at a working temperature of T^W and fully damaged chemically disordered state after large radiation damage with high bombardment rate, respectively. The initial CSRO parameter is $\alpha_{1I} = \alpha_1^E(T^W)$, and then the bombardments start with an interval Δt . At each bombardment, the CSRO structure is destroyed and then the CSRO parameter decreases by a certain amount $\Delta\alpha_1^B$. Here, we assume that $\Delta\alpha_1^B$ is constant. The damage rate can be defined as $\dot{\alpha}_1^D = \Delta\alpha_1^B/\Delta t$. By i th bombardment, the CSRO parameter changes from α_{1I}^i to α_{1E}^i (the vertical red lines in Fig. 11 (a)), where $\alpha_{1E}^i = \max\{\alpha_{1I}^i - \Delta\alpha_1^B, \alpha_1^D\}$ because α_1 cannot fall below α_1^D . Whenever $\alpha_{1E}^i < \alpha_1^E$, the diffusion healing of CSRO occurs (the curved green lines in Fig. 11 (a)). The healing rate can be written as $\dot{\alpha}_1^H = \overline{\Delta\alpha N^I} \nu_0 \exp\left[\frac{-\Delta G(T^W)}{k_B T^W}\right]$, where $\overline{\Delta\alpha}$ is the average of change in α_1 by each interstitial jump once in a material with N atoms, N^I is the total number of interstitials in this material, $\nu_0 \approx 1 \times 10^{13} \text{ s}^{-1}$ is trial frequency of the interstitial jump, k_B is the Boltzmann constant, and $\Delta G(T^W)$ is apparent activation free energy of the interstitial jump. Therefore, the CSRO parameter at time t after the first bombardment ($t = 0$) can be predicted by the following equation:

$$\alpha_1(t) = \alpha_1^E(T^W) - \sum_i^{N^B} (\alpha_{1I}^i - \alpha_{1E}^i) + \overline{\Delta\alpha} N^I \nu_0 \exp\left[\frac{-\Delta G(T^W)}{k_B T^W}\right] \quad (5)$$

where $N^B = \text{int}(t/\Delta t) + 1$ is the number of bombardments up to time t . According to Eq. (5), it is obvious that the competition mainly depends on the working temperature T^W and bombardment intensity $\Delta\alpha_1^B$ and interval Δt .

Fig. 11(b) and (c) show the CSRO parameter changes calculated by Eq. (5) in two different cases at the working temperature $T^W = 1100 \text{ K}$, such as damage rate $\dot{\alpha}_1^D$ dominant: CSRO destroy (b) and healing rate $\dot{\alpha}_1^H$ dominant: CSRO preserve (c), as shown in Fig. 11(d). Here we set the equilibrium CSRO state α_1^E and chemical disordered state α_1^D to 0.5 and 0.2, respectively [37 12]. The apparent activation free energy of interstitial jump $\Delta G(T^W)$ is found in the Supplementary Information Fig. S4. According to our previous study, in the model with 256,000 atoms, the average of CSRO change $\overline{\Delta\alpha}$ by each interstitial jump once is calculated as 10^{-5} , the defect concentration in the equilibrium state is 0.4 %, and the $\Delta\alpha_1^B$ is a constant of 0.006 [57]. When $\dot{\alpha}_1^H > \dot{\alpha}_1^D$, the existence of the CSRO structure can be maintained for an extended period, thus better radiation resistance can be maintained.

5. Conclusions

We have investigated the chemical ordering effect on the radiation resistance of a CoNiCrFeMn high-entropy alloy using combined atomic simulations that included MC and MD simulations. Our results showed that the annealing temperature of the alloys, which leads to temperature dependent chemical ordering, strongly influences the radiation resistance of CoNiCrFeMn at low dpa radiation. Annealing at 600 K, phase decomposition led to the formation of an initial stage Cr-rich region,

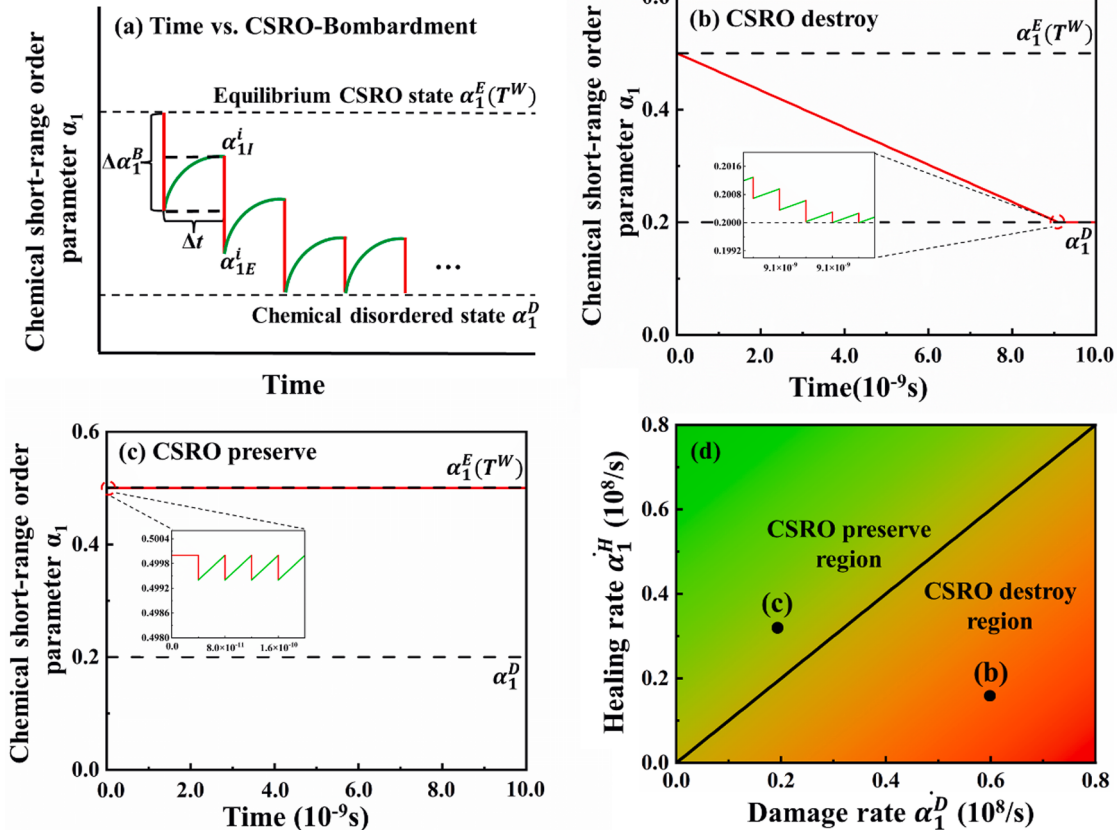


Fig. 11. (a) Schematic Time vs CSRO-Bombardment curve (See the main text for the details), (b) CSRO destroy case, and (c) CSRO preserve case. (d) Relationship between the healing rate $\dot{\alpha}_1^H$ and damage rate $\dot{\alpha}_1^D$. “(b)” and “(c)” are showing the condition used to compute figures (b) and (c), respectively.

which accelerated the aggregation and the evolution of defects. The Cr-rich region facilitated the formation of dislocation loops, thereby reducing the radiation resistance of CoNiCrFeMn. Annealing at 1100 K, a CSRO structure was formed, leading to several key radiation resistance mechanisms, such as a delay of defect number growth, dislocation density decrease, and lower defect diffusivity. In addition, we proposed a CSRO radiation damage – diffusion healing competition model, which demonstrates that the CSRO and the key anti-damage mechanisms can be maintained at the working temperature of 1100 K under a relatively lower damage rate. If we can tune the CSRO formation temperature to the working temperature by controlling the chemical composition of a HEA, we may obtain high radiation resistance for an extended period. Finally, we should note that the kinetics of the CSRO diffusion healing is not demonstrated in our simulation because of the time scale limitation of MD method. Therefore, unfortunately, the competition model's prediction is not supported by the atomistic simulations. A direct atomistic simulation of the damage-healing competition must be a challenge for the future.

6. Data availability

The data that support the findings of this study are available from the corresponding author upon reasonable request.

CRediT authorship contribution statement

Yangen Li: Methodology, Software, Formal analysis, Writing – original draft. **Jun-Ping Du:** Software, Methodology. **Peijun Yu:** Methodology, Software. **Rui Li:** Methodology, Software. **Shuhei Shinzato:** Methodology, Software. **Qing Peng:** Methodology, Formal analysis. **Shigenobu Ogata:** Conceptualization, Writing – review & editing, Supervision, Project administration.

Declaration of Competing Interest

The authors declare that they have no known competing financial interests or personal relationships that could have appeared to influence the work reported in this paper.

Data availability

Data will be made available on request.

Acknowledgments

This work was supported by Element Strategy Initiative for Structural Materials of MEXT, Grant Number JPMXP0112101000. Y.L. acknowledges the support by the JST SPRING, Grant Number JPMJSP2138. Y.L. and S.O. acknowledge the Center for Computational Materials Science, IMR, Tohoku University for the use of MASAMUNE-IMR and the large-scale computer systems at the Cybermedia Center, Osaka University. R.L. acknowledges the support provided by the Fundamental Research funds for the Central Universities through project FRF-AT-20-09. Q.P. acknowledges the support by LiYing Program of the Institute of Mechanics, Chinese Academy of Science through Grant No. E1Z1011001. P.Y. and S.O. acknowledge the support by the JSPS KAKENHI Grant Nos. JP18H05450 and JP18H05453, S.O. acknowledges the support by the JSPS KAKENHI Grant Nos. JP17H01238 and JP17K18827.

Appendix A. Supplementary material

Supplementary data to this article can be found online at <https://doi.org/10.1016/j.commatsci.2022.111764>.

References

- [1] E.P. George, D. Raabe, R.O. Ritchie, High-entropy alloys, *Nat. Rev. Mater.* 4 (2019) 515–534.
- [2] Y.H. Jo, S. Jung, W.M. Choi, S.S. Sohn, H.S. Kim, B.J. Lee, N.J. Kim, S. Lee, Cryogenic strength improvement by utilizing room-temperature deformation twinning in a partially recrystallized VCrMnFeCoNi high-entropy alloy, *Nat. Commun.* 8 (2017) 1–8.
- [3] M.H. Tsai, Physical properties of high entropy alloys, *Entropy*. 15 (2013) 5338–5345.
- [4] Z. Li, K.G. Pradeep, Y. Deng, D. Raabe, C.C. Tasan, Metastable high-entropy dual-phase alloys overcome the strength-ductility trade-off, *Nature*. 534 (2016) 227–230.
- [5] F. Otto, A. Dlouhý, C. Somsen, H. Bei, G. Eggeler, E.P. George, The influences of temperature and microstructure on the tensile properties of a CoCrFeMnNi high-entropy alloy, *Acta Mater.* 61 (2013) 5743–5755.
- [6] Z. Li, S. Zhao, R.O. Ritchie, M.A. Meyers, Mechanical properties of high-entropy alloys with emphasis on face-centered cubic alloys, *Prog. Mater. Sci.* 102 (2019) 296–345.
- [7] C.E. Slone, J. Miao, E.P. George, M.J. Mills, Achieving ultra-high strength and ductility in equiatomic CrCoNi with partially recrystallized microstructures, *Acta Mater.* 165 (2019) 496–507.
- [8] K. Xiang, L.Y. Chen, L. Chai, N. Guo, H. Wang, Microstructural characteristics and properties of CoCrFeNiNb_x high-entropy alloy coatings on pure titanium substrate by pulsed laser cladding, *Appl. Surf. Sci.* 517 (2020), 146214.
- [9] B. Yin, F. Maresca, W.A. Curtin, Vanadium is an optimal element for strengthening in both fcc and bcc high-entropy alloys, *Acta Mater.* 188 (2020) 486–491.
- [10] Q. Ding, Y. Zhang, X. Chen, X. Fu, D. Chen, S. Chen, L. Gu, F. Wei, H. Bei, Y. Gao, M. Wen, J. Li, Z. Zhang, T. Zhu, R.O. Ritchie, Q. Yu, Tuning element distribution, structure and properties by composition in high-entropy alloys, *Nature* 574 (2019) 223–227.
- [11] Z. Lei, X. Liu, Y. Wu, H. Wang, S. Jiang, S. Wang, X. Hui, Y. Wu, B. Gault, P. Kontis, D. Raabe, L. Gu, Q. Zhang, H. Chen, H. Wang, J. Liu, K. An, Q. Zeng, T.G. Nieh, Z. Lu, Enhanced strength and ductility in a high-entropy alloy via ordered oxygen complexes, *Nature* 563 (2018) 546–550.
- [12] E. Antillon, C. Woodward, S.I. Rao, B. Akdim, T.A. Parthasarathy, Chemical short range order strengthening in a model FCC high entropy alloy, *Acta Mater.* 190 (2020) 29–42.
- [13] O. El-Atwani, N. Li, M. Li, A. Devaraj, J.K.S. Baldwin, M.M. Schneider, D. Sobieraj, J.S. Wróbel, D. Nguyen-Manh, S.A. Maloy, E. Martinez, Outstanding radiation resistance of tungsten-based high-entropy alloys, *Sci. Adv.* 5 (2019) eaav2002.
- [14] C. Lu, T. Yang, K. Jin, N. Gao, P. Xiu, Y. Zhang, F. Gao, H. Bei, W.J. Weber, K. Sun, Y. Dong, L. Wang, Radiation-induced segregation on defect clusters in single-phase concentrated solid-solution alloys, *Acta Mater.* 127 (2017) 98–107.
- [15] C. Lu, L. Niu, N. Chen, K. Jin, T. Yang, P. Xiu, Y. Zhang, F. Gao, H. Bei, S. Shi, M. R. He, I.M. Robertson, W.J. Weber, L. Wang, Enhancing radiation tolerance by controlling defect mobility and migration pathways in multicomponent single-phase alloys, *Nat. Commun.* 7 (2016) 1–8.
- [16] Y. Li, R. Li, Q. Peng, S. Ogata, Reduction of dislocation, mean free path, and migration barriers using high entropy alloy: Insights from the atomistic study of irradiation damage of CoNiCrFeMn, *Nanotechnology* 31 (2020) 8.
- [17] K.Y. Tsai, M.H. Tsai, J.W. Yeh, Sluggish diffusion in Co-Cr-Fe-Mn-Ni high-entropy alloys, *Acta Mater.* 61 (2013) 4887–4897.
- [18] E. Levo, F. Granberg, C. Fridlund, K. Nordlund, F. Djurabekova, Radiation damage buildup and dislocation evolution in Ni and equiatomic multicomponent Ni-based alloys, *J. Nucl. Mater.* 490 (2017) 323–332.
- [19] J. Dąbrowska, M. Danielewski, State-of-the-art diffusion studies in the high entropy alloys, *Met.* 10 (2020) 347.
- [20] E.J. Pickering, A.W. Carruthers, P.J. Barron, S.C. Middleburgh, D.E.J. Armstrong, A.S. Gandy, High-entropy alloys for advanced nuclear applications, *Entropy* 23 (2021) 98.
- [21] Q. Xu, H.Q. Guan, Z.H. Zhong, S.S. Huang, J.J. Zhao, Irradiation resistance mechanism of the CoCrFeMnNi equiatomic high-entropy alloy, *Sci. Rep.* 11 (2021) 1–8.
- [22] H.S. Do, B.J. Lee, Origin of radiation resistance in multi-principal element alloys, *Sci. Rep.* 8 (2018) 1–9.
- [23] Z. Wu, H. Bei, G.M. Pharr, E.P. George, Temperature dependence of the mechanical properties of equiatomic solid solution alloys with face-centered cubic crystal structures, *Acta Mater.* 81 (2014) 428–441.
- [24] K.V.S. Thurston, B. Gludovatz, A. Hohenwarter, G. Laplanche, E.P. George, R. O. Ritchie, Effect of temperature on the fatigue-crack growth behavior of the high-entropy alloy CrMnFeCoNi, *Intermetallics*. 88 (2017) 65–72.
- [25] F. Otto, A. Dlouhý, K.G. Pradeep, M. Kuběnová, D. Raabe, G. Eggeler, E.P. George, Decomposition of the single-phase high-entropy alloy CrMnFeCoNi after prolonged anneals at intermediate temperatures, *Acta Mater.* 112 (2016) 40–52.
- [26] F. He, Z. Wang, Q. Wu, J. Li, J. Wang, C.T. Liu, Phase separation of metastable CoCrFeNi high entropy alloy at intermediate temperatures, *Ser. Mater.* 126 (2017) 15–19.
- [27] G. Laplanche, S. Berglund, C. Reinhart, A. Kostka, F. Fox, E.P. George, Phase stability and kinetics of σ-phase precipitation in CrMnFeCoNi high-entropy alloys, *Acta Mater.* 161 (2018) 338–351.
- [28] F.X. Zhang, S. Zhao, K. Jin, H. Xue, G. Velisa, H. Bei, R. Huang, J.Y.P. Ko, D. C. Pagan, J.C. Neufeind, W.J. Weber, Y. Zhang, Local Structure and Short-Range Order in a NiCoCr Solid Solution Alloy, *Phys. Rev. Lett.* 118 (2017), 205501.

- [29] R. Zhang, S. Zhao, C. Ophus, Y. Deng, S.J. Vachhani, B. Ozdol, R. Traylor, K. C. Bustillo, J.W. Morris, D.C. Chrzan, M. Asta, A.M. Minor, Direct imaging of short-range order and its impact on deformation in Ti-6Al, *Sci. Adv.* 5 (2019) eaax2799.
- [30] Y. Wu, F. Zhang, X. Yuan, H. Huang, X. Wen, Y. Wang, M. Zhang, H. Wu, X. Liu, H. Wang, S. Jiang, Z. Lu, Short-range ordering and its effects on mechanical properties of high-entropy alloys, *J. Mater. Sci. Technol.* 62 (2021) 214–220.
- [31] Q.J. Li, H. Sheng, E. Ma, Strengthening in multi-principal element alloys with local-chemical-order roughened dislocation pathways, *Nat. Commun.* 10 (2019) 1–11.
- [32] S. Yin, J. Ding, M. Asta, R.O. Ritchie, Ab initio modeling of the energy landscape for screw dislocations in body-centered cubic high-entropy alloys, *Npj Comput. Mater.* 6 (2020) 1–11.
- [33] J. Ding, Q. Yu, M. Asta, R.O. Ritchie, Tunable stacking fault energies by tailoring local chemical order in CrCoNi medium-entropy alloys, *Proc. Natl. Acad. Sci. U. S. A.* 115 (2018) 8919–8924.
- [34] R. Zhang, S. Zhao, J. Ding, Y. Chong, T. Jia, C. Ophus, M. Asta, R.O. Ritchie, A. M. Minor, Short-range order and its impact on the CrCoNi medium-entropy alloy, *Nature* 581 (2020) 283–287.
- [35] S. Zhao, Y. Ossetsky, Y. Zhang, Diffusion of point defects in ordered and disordered Ni-Fe alloys, *J. Alloys Compd.* 805 (2019) 1175–1183.
- [36] K. Vörtsler, N. Juslin, G. Bonny, L. Malerba, K. Nordlund, The effect of prolonged irradiation on defect production and ordering in FeCr and FeNi alloys, *J. Phys. Condens. Matter.* 23 (2011), 355007.
- [37] L. Koch, F. Granberg, T. Brink, D. Utt, K. Albe, F. Djurabekova, K. Nordlund, Local segregation versus irradiation effects in high-entropy alloys: Steady-state conditions in a driven system, *J. Appl. Phys.* 122 (2017), 105106.
- [38] Q. Peng, F. Meng, Y. Yang, C. Lu, H. Deng, L. Wang, S. De, F. Gao, Shockwave generates $< 100 >$ dislocation loops in bcc iron, *Nat. Commun.* 9 (9) (2018) 2018., 1–6.
- [39] S.G. Louie, Y.-H. Chan, F.H. da Jornada, Z. Li, D.Y. Qiu, Discovering and understanding materials through computation, *Nat. Mater.* 20 (2021) 728–735.
- [40] W.M. Choi, Y.H. Jo, S.S. Sohn, S. Lee, B.J. Lee, Understanding the physical metallurgy of the CoCrFeMnNi high-entropy alloy: An atomistic simulation study, *Npj Comput. Mater.* 4 (2018) 1.
- [41] E. Zarkadoula, G. Samolyuk, W.J. Weber, Two-temperature model in molecular dynamics simulations of cascades in Ni-based alloys, *J. Alloys Compd.* 700 (2017) 106–112.
- [42] A. Stukowski, Visualization and analysis of atomistic simulation data with OVITO—the Open Visualization Tool, *Model. Simul. Mater. Sci. Eng.* 18 (2009), 015012.
- [43] A. Stukowski, Structure identification methods for atomistic simulations of crystalline materials, *Model. Simul. Mater. Sci. Eng.* 20 (2012), 045021.
- [44] A. Stukowski, V.V. Bulatov, A. Arsenlis, Automated identification and indexing of dislocations in crystal interfaces, *Model. Simul. Mater. Sci. Eng.* 20 (2012), 085007.
- [45] D. de Fontaine, The number of independent pair-correlation functions in multicomponent systems, *J. Appl. Crystallogr.* 4 (1971) 15–19.
- [46] S. Guo, H. Chen, M. Wang, Research on the dislocation differences of CoCrFeMnNi with different local chemical orders during room temperature tensile test, *J. Alloys Compd.* 868 (2021), 159215.
- [47] S. Plimpton, Fast parallel algorithms for short-range molecular dynamics, *J. Comput. Phys.* 117 (1995) 1–19.
- [48] H.J.C. Berendsen, J.P.M. Postma, W.F. Van Gunsteren, A. Dinola, J.R. Haak, Molecular dynamics with coupling to an external bath, *J. Chem. Phys.* 81 (1998) 3684.
- [49] M.W. Ullah, D.S. Aidhy, Y. Zhang, W.J. Weber, Damage accumulation in ion-irradiated Ni-based concentrated solid-solution alloys, *Acta Mater.* 109 (2016) 17–22.
- [50] M.W. Ullah, H. Xue, G. Velisa, K. Jin, H. Bei, W.J. Weber, Y. Zhang, Effects of chemical alternation on damage accumulation in concentrated solid-solution alloys, *Sci. Reports* 71 (7) (2017) 1–11.
- [51] F. Granberg, K. Nordlund, M.W. Ullah, K. Jin, C. Lu, H. Bei, L.M. Wang, F. Djurabekova, W.J. Weber, Y. Zhang, Mechanism of Radiation Damage Reduction in Equiatomic Multicomponent Single Phase Alloys, *Phys. Rev. Lett.* 116 (2016), 135504.
- [52] H. Mehrer, Diffusion in solids: fundamentals, methods, materials, diffusion-controlled processes, Springer Science & Business Media, 2007.
- [53] H. Guan, S. Huang, J. Ding, F. Tian, Q. Xu, J. Zhao, Chemical environment and magnetic moment effects on point defect formations in CoCrNi-based concentrated solid-solution alloys, *Acta Mater.* 187 (2020) 122–134.
- [54] G. Henkelman, H. Jónsson, Improved tangent estimate in the nudged elastic band method for finding minimum energy paths and saddle points, *J. Chem. Phys.* 113 (2000) 9978.
- [55] G. Henkelman, B.P. Uberuaga, H. Jónsson, A climbing image nudged elastic band method for finding saddle points and minimum energy paths, *J. Chem. Phys.* 113 (2000) 9901.
- [56] Y. Ossetsky, A.V. Barashev, L.K. Béland, Z. Yao, K. Ferasat, Y. Zhang, Tunable chemical complexity to control atomic diffusion in alloys, *Npj Comput. Mater.* 6 (6) (2020) 2020., 1–8.
- [57] Z. Shen, J.-P. Du, S. Shinzato, Y. Sato, P. Yu, S. Ogata, Kinetic Monte Carlo simulation framework for chemical short-range order formation kinetics in a multi-principal-element alloy, *Comput. Mater. Sci.* 198 (2021), 110670.